

We are IntechOpen, the world's leading publisher of Open Access books Built by scientists, for scientists

7,000

Open access books available

186,000

International authors and editors

200M

Downloads

Our authors are among the

154

Countries delivered to

TOP 1%

most cited scientists

12.2%

Contributors from top 500 universities



WEB OF SCIENCE™

Selection of our books indexed in the Book Citation Index
in Web of Science™ Core Collection (BKCI)

Interested in publishing with us?
Contact book.department@intechopen.com

Numbers displayed above are based on latest data collected.
For more information visit www.intechopen.com



Image Fusion Using a Parameterized Logarithmic Image Processing Framework

Sos S. Agaian¹, Karen A. Panetta² and Shahan C. Nercessian²

¹University of Texas at San Antonio

²Tufts University
USA

1. Introduction

Advances in sensor technology have brought about extensive research in the field of image fusion. Image fusion is the combination of two or more source images which vary in resolution, instrument modality, or image capture technique into a single composite representation (Hill et al., 2002). Thus, the source images are complementary in many ways, with no one input image being an adequate data representation of the scene. Therefore, the goal of an image fusion algorithm is to integrate the redundant and complementary information obtained from the source images in order to form a new image which provides a better description of the scene for human or machine perception (Kumar & Dass, 2009). Image fusion is essential for computer vision and robotics systems in which fusion results can be used to aid further processing steps for a given task. Image fusion techniques are practical and fruitful for many applications, including medical imaging, security, military, remote sensing, digital camera and consumer use. There are many cases in medical imaging where viewing a series of images individually is not convenient. For example, magnetic resonance imaging (MRI) and computed tomography (CT) images provide structural and anatomical information with high resolution. Positron emission tomography (PET) and single photon emission computed tomography (SPECT) images provide functional information with low resolution. Therefore, the fusion of MRI or CT images with PET or SPECT images can provide the needed structural, anatomical, and functional information for medical diagnosis, anomaly detection and quantitative analysis (Daneshvar & Ghassemian, 2010). Moreover, the combination of MRI and CT images can provide images containing both dense bone structure and soft tissue information (Yang et al., 2010). Similarly, the combination of MRI-T1 images provides greater details of anatomical structures while MRI-T2 images provides greater contrast between normal and abnormal tissue matter, and thus, their fusion can also help to extract the features needed by physicians (Wang, 2008). In security applications, thermal/infrared images provide information regarding the presence of intruders or potential threat objects (Zhang & Blum, 1997). For military applications, such images can also provide terrain clues for helicopter navigation. Visible light images provide high-resolution structural information based on the way in which light is reflected. Thus, the fusion of thermal/infrared and visible images can be used to aid navigation, concealed weapon detection, and surveillance/border patrol by

humans or automated computer vision security systems (Qiong et al., 2008). In remote sensing applications, the fusion of multi-spectral low-resolution remote sensing images with a high-resolution panchromatic image can yield a high-resolution multispectral image with good spectral and spatial characteristics (Chibani, 2005). As a visible light image is taken by a CCR device at a given focal point, certain objects in the image may be in focus while others may be blurred and out of focus. For digital camera applications and consumer use, the fusion of images taken at different focal points can essentially create an image having multiple focal points in which all objects in the scene are in focus (Zhang, 1999).

The most basic of image fusion approaches include spatial domain techniques using simple averaging, Principal Component Analysis (PCA) (Chavez & Kwarteng, 1989), and the Intensity-Hue-Saturation (IHS) transformation (Tu et al., 2001). However, such methods do not incorporate aspects of the human visual system in their formulation. It is well known that the human visual system is particularly sensitive to edges at their various scales (Tabb & Ahuja, 1997). Based on this fact, multi-resolution image fusion techniques have been proposed in order to yield more visually accurate fusion results. These approaches decompose image signals into low-pass and high-pass coefficients via a multi-resolution decomposition scheme, fuse low-pass and high-pass coefficients according to specific fusion rules, and perform an inverse transform to yield the final fusion result. The use of different fusion rules for low-pass and high-pass coefficients provides a means of yielding fusion results inspired by the human visual system. Pixel-based image fusion algorithms fuse detail coefficients pixels individually based on either selection or weighted averaging. Motivated by the fact that applications requiring image fusion are interested in integrating information at the feature level, region-based image fusion algorithms use segmentation to extract regions corresponding to perceived objects from the source images, and fuse regions according to a region activity measure (Piella, 2003). Because of their general formulations, both pixel- and region-based fusion rules can be adopted using any multi-resolution decomposition technique, allowing for a convenient means of comparing the performance of multi-resolution decomposition schemes for image fusion while keeping the fusion rules constant. The most common of multi-resolution decomposition schemes for image fusion have been the pyramid transforms and wavelet transforms. Particularly, pixel- and region-based image fusion algorithms using the Laplacian Pyramid (LP) (Burt & Adelson, 1983), Discrete Wavelet Transform (DWT) (Mallat, 1989), and Stationary Wavelet Transform (SWT) (Rockinger, 1997) have been proposed.

Although much of the research in image fusion has strived to formulate effective image fusion techniques which are consistent with the human visual system, the mentioned multi-resolution decomposition schemes and their respective image fusion algorithms are implemented using standard arithmetic operators which are not suitable for processing images. Conversely, the Logarithmic Image Processing (LIP) model was proposed to provide a nonlinear framework for visualizing images using a mathematically rigorous arithmetical structure specifically designed for image manipulation (Jourlin & Pinoli, 2001). The LIP model views images in terms of their graytone functions, which are interpreted as absorption filters. It processes graytone functions using a new arithmetic which replaces standard arithmetical operators. The resulting set of arithmetic operators can be used to process images based on a physically relevant image formation model. The model makes use of a logarithmic isomorphic transformation, consistent with the fact that the human visual system processes light logarithmically. The model has also shown to satisfy Weber's

Law, which quantifies the human eye's ability to perceive intensity differences for a given background intensity (Pinoli, 1998). As a result, image enhancement, edge detection, and image restoration algorithms utilizing the LIP model have yielded better results (Deng et al., 2009; Debayle et al., 2006).

However, an unfortunate consequence of the LIP model for general practical purposes is that the dynamic range of the processed image data is left unchanged causing information loss and signal clipping. Moreover, specifically for image fusion purposes, the combination of source images in regions of vastly different mean intensity yield visually poor results even though their processing is motivated by a relevant physical model. It is therefore advantageous to formulate a generalized image processing framework which is able to effectively unify the LIP and standard processing frameworks into a single framework. Consequently, the Parameterized Logarithmic Image Processing (PLIP) model was formulated. The PLIP model is a generalization of the LIP model which attempts to overcome the mentioned shortcomings of the standard processing and LIP models and can yield visually more pleasing outputs (Panetta et al., 2008). A mathematical analysis shows that in fact LIP and standard mathematical operators are instances of the generalized PLIP framework. Adaptations of edge detection and image enhancement algorithms using the PLIP model have demonstrated the improved performance achieved by the parameterized framework (Panetta et al., 2007; Wharton et al. 2008). In this chapter, we investigate the use of the PLIP model for image fusion applications. New multi-resolution decomposition schemes and image fusion rules using the PLIP model are introduced, and consequently, new pixel- and region-based image fusion algorithms using the PLIP model are proposed.

The remainder of this chapter is organized as follows: Section 2 provides a brief overview of commonly used multi-scale image decomposition techniques. Section 3 provides background information for pixel-based image fusion algorithms, while Section 4 provides background information for region-based image fusion algorithms. Section 5 describes the LIP and PLIP models, and in particular, analyzes the advantageous properties of the proposed PLIP model. Section 6 subsequently introduces the proposed multi-scale image decomposition techniques and image fusion algorithms. Section 7 describes the quality metric used for quantitative assessment of image fusion quality. Section 8 compares the proposed image fusion algorithms with existing standards via computer simulations. Section 9 draws conclusions based on the presented experimental results.

2. Multi-resolution image decomposition schemes

2.1 Laplacian Pyramid (LP)

The LP uses the Gaussian Pyramid to provide a multi-resolution image representation for an image I (Burt & Adelson, 1983). Analysis and synthesis using the LP is illustrated in Figure 1. Each analysis stage consists of low-pass filtering, down-sampling, interpolating, and differencing steps in order to generate the approximation coefficients $y_0^{(n)}$ and detail coefficients $y_1^{(n)}$ at scale n . The approximation coefficients at a scale $n > 0$ are generated by

$$y_0^{(n)} = \left[w * y_0^{(n-1)} \right]_{\downarrow 2} \quad (1)$$

where $y_0^{(0)} = I$ and w is a 2D low-pass filter, usually defined as

$$w = \frac{1}{256} \begin{bmatrix} 1 & 4 & 6 & 4 & 1 \\ 4 & 16 & 24 & 16 & 4 \\ 6 & 24 & 36 & 24 & 6 \\ 4 & 16 & 24 & 16 & 4 \\ 1 & 4 & 6 & 4 & 1 \end{bmatrix} \quad (2)$$

The detail coefficients at scale n are consequently calculated as a weighted difference between successive levels of the Gaussian Pyramid, and is given by

$$y_1^{(n)} = y_0^{(n)} - 4w * [y_0^{(n+1)}]_{\uparrow 2} \quad (3)$$

The synthesis procedure begins from the approximation coefficient at the high decomposition level N . Each synthesis level reconstructs approximation coefficients at a scale $n < N$ by

$$y_0^{(n)} = y_1^{(n)} + 4w * [y_0^{(n+1)}]_{\uparrow 2} \quad (4)$$

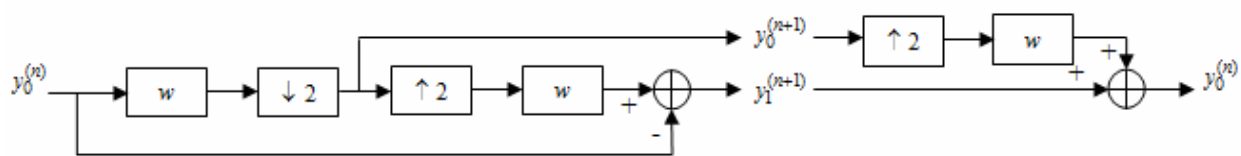


Fig. 1. Laplacian Pyramid analysis and synthesis

2.2 Discrete Wavelet Transform (DWT)

The 2D separable DWT uses a quadrature mirror set of 1D filters to provide a multi-resolution scheme for an image I with added directionality relative to the LP (Mallat, 1989). Analysis and synthesis using the DWT is illustrated in Figure 2. The DWT is able to provide perfect reconstruction while using critical sampling. Each analysis stage consists of filtering along rows, down-sampling along columns, filtering along columns, and down-sampling along rows in order to generate the approximation coefficient sub-band $y_0^{(n)}$ and detail coefficient sub-bands $y_1^{(n)}$, $y_2^{(n)}$, and $y_3^{(n)}$ at scale n . Given a 1D low-pass wavelet analysis filter g and a 1D low-pass wavelet analysis filter h , the approximation coefficients at a scale $n > 0$ are generated by

$$y_0^{(n)} = \left[g_C * \left[g_R * y_0^{(n-1)} \right]_{\downarrow 2_C} \right]_{\downarrow 2_R} \quad (5)$$

where $y_0^{(0)} = I$, and the subscripts R and C denote operations performed along rows and columns, respectively. Similarly, the detail coefficients at scale n are calculated by

$$y_1^{(n)} = \left[h_C * \left[g_R * y_0^{(n-1)} \right]_{\downarrow 2_C} \right]_{\downarrow 2_R} \quad (6)$$

$$y_2^{(n)} = \left[g_C * \left[h_R * y_0^{(n-1)} \right] \downarrow_{2_C} \right] \downarrow_{2_R} \quad (7)$$

$$y_3^{(n)} = \left[h_C * \left[h_R * y_0^{(n-1)} \right] \downarrow_{2_C} \right] \downarrow_{2_R} \quad (8)$$

and are oriented horizontally, vertically, and diagonally, respectively. The synthesis procedure begins from the wavelet coefficients at the highest decomposition level N . Filtering and up-sampling steps are performed in order to perfectly reconstruct the image signal. Each synthesis level reconstructs approximation coefficients at a scale $n < N$ by

$$y_0^{(n)} = \hat{g}_R * \left[\hat{g}_C * \left[y_0^{(n+1)} \right] \uparrow_{2_R} + \hat{h}_C * \left[y_1^{(n+1)} \right] \uparrow_{2_R} \right] \uparrow_{2_C} + \hat{h}_R * \left[\hat{g}_C * \left[y_2^{(n+1)} \right] \uparrow_{2_R} + \hat{h}_C * \left[y_3^{(n+1)} \right] \uparrow_{2_R} \right] \uparrow_{2_C} \quad (9)$$

where \hat{g} and \hat{h} are 1D low-pass and high-pass wavelet synthesis filters, respectively.

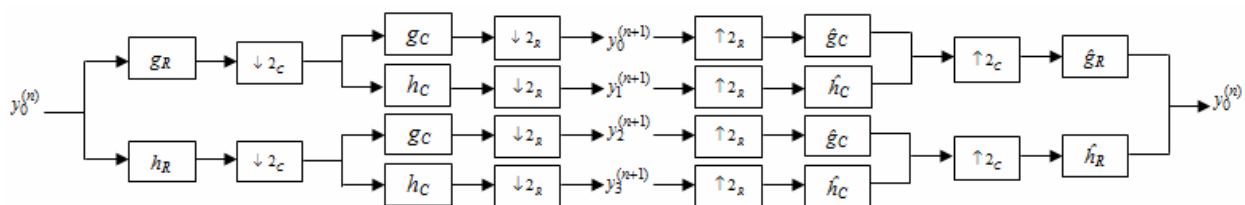


Fig. 2. Discrete Wavelet Transform analysis and synthesis

2.3 Discrete Wavelet Transform (SWT)

Both the DWT and LP are shift-variant due to the down-sampling step which they employ. Therefore, the alteration of transform coefficients may introduce artifacts when processed using the DWT and to a lesser extent, the LP. It can introduce artifacts into the fusion results particularly for cases in which source images are misregistered. The SWT is a shift-invariant, redundant wavelet transform which attempts to reduce artifact effects by up-sampling analysis filters rather than down-sampling approximation images at each level of decomposition (Fowler, 2005). Therefore, each analysis stage calculates the approximation coefficient sub-band $y_0^{(n)}$ and detail coefficient sub-bands $y_1^{(n)}$, $y_2^{(n)}$, and $y_3^{(n)}$ at scale n by

$$y_0^{(n)} = g_C^{(n)} * g_R^{(n)} * y_0^{(n-1)} \quad (10)$$

$$y_1^{(n)} = h_C^{(n)} * g_R^{(n)} * y_0^{(n-1)} \quad (11)$$

$$y_2^{(n)} = g_C^{(n)} * h_R^{(n)} * y_0^{(n-1)} \quad (12)$$

$$y_3^{(n)} = h_C^{(n)} * h_R^{(n)} * y_0^{(n-1)} \quad (13)$$

where

$$g^{(n)} = \left[g^{(n-1)} \right]_{\uparrow 2} \quad (14)$$

$$h^{(n)} = \left[h^{(n-1)} \right]_{\uparrow 2} \quad (15)$$

and $g^{(0)} = g, h^{(0)} = h$.

3. Pixel-based fusion using multi-resolution decomposition schemes

A generalized pixel-based multi-resolution image fusion algorithm is illustrated in Figure 3. The input source images are transformed using a given multi-resolution image decomposition technique T . One fusion rule is used to fuse the approximation coefficients at the highest decomposition level. A second fusion rule is used to fuse the detail coefficients at each decomposition level. The resulting inverse transform yields the final fused result. Although image fusion algorithms are expected to withstand minor registration differences, the source images to be fused are assumed to be registered.

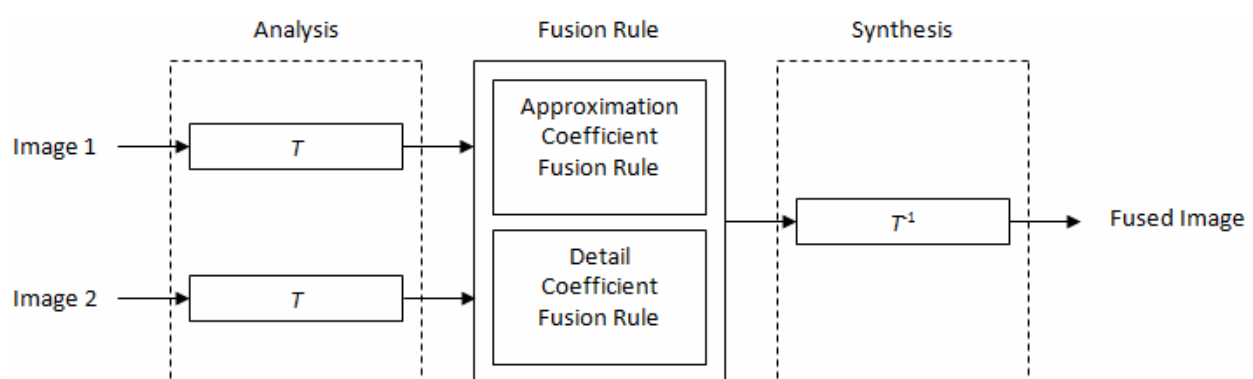


Fig. 3. A generalized pixel-based multi-resolution image fusion algorithm

Misregistered source images should be subjected to registration preprocessing steps independent to the image fusion algorithm. The approximation coefficients at the highest level of decomposition N are most commonly fused via uniform averaging. This is because at the highest level of decomposition, the approximation coefficients are interpreted as the mean intensity value of the source images with all salient features encapsulated by the detail coefficient sub-bands at their various scales (Piella, 2003). Therefore, fusing approximation coefficients at their highest level of decomposition by averaging maintains the appropriate mean intensity needed for the fusion result with minimal loss of salient features. Given $y_{I_1,0}^{(N)}$ and $y_{I_2,0}^{(N)}$, the approximation coefficient sub-bands of images I_1 and I_2 , respectively, at the highest decomposition level N , the approximation coefficients for the fused image F at the highest level of decomposition is given by

$$y_{F,0}^{(N)} = \frac{y_{I_1,0}^{(N)} + y_{I_2,0}^{(N)}}{2} \quad (16)$$

Conversely, the detail coefficients of the source images correspond to salient features such as lines and edges detected at various scales. Therefore, fusion rules for detail coefficients at

each decomposition level should be formulated in order to preserve these features. Such fusion rules are inspired by the human visual system, which is particularly sensitive to edges. Many pixel-based detail coefficient fusion rules have been proposed. In this work, two common detail coefficient fusion rules are considered.

3.1 Absolute maximum detail coefficient fusion rule

The absolute maximum (AM) detail coefficient fusion rule selects the detail coefficient in each sub-band with greatest magnitude (Piella, 2003). For each of the i high-pass sub-bands at each level of decomposition n , the multiplicative weights for fusion are given by

$$\lambda_i^{(n)}(k, l) = \begin{cases} 1 & |y_{l_1, i}^{(n)}(k, l)| > |y_{l_2, i}^{(n)}(k, l)| \\ 0 & |y_{l_1, i}^{(n)}(k, l)| \leq |y_{l_2, i}^{(n)}(k, l)| \end{cases} \quad (17)$$

For each of the i high-pass sub-bands at each level of decomposition n , the detail coefficients of the fused image F are determined by

$$y_{F, i}^{(n)}(k, l) = \lambda_i^{(n)}(k, l) y_{l_1, i}^{(n)}(k, l) + (1 - \lambda_i^{(n)}(k, l)) y_{l_2, i}^{(n)}(k, l) \quad (18)$$

3.2 Burt and Kolczynski's detail coefficient fusion rule

Burt and Kolczynski's (BK) detail coefficient fusion rule combines detail coefficients based on an activity and match measure (Burt & Kolczynski, 1993). The activity measure for each $w \times w$ local window of each sub-band i is calculated for each source image, given as

$$a_{l, i}^{(n)}(k, l) = \sum_{(\Delta k, \Delta l) \in W} \left(y_{l, i}^{(n)}(k + \Delta k, l + \Delta l) \right)^2 \quad (19)$$

The local match measure of each sub-band measures the correlation of each sub-band between source images, and is given as

$$m_{l_1, l_2, i}^{(n)}(k, l) = \frac{2 \sum_{(\Delta k, \Delta l) \in W} \left(y_{l_1, i}^{(n)}(k + \Delta k, l + \Delta l) \right) \left(y_{l_2, i}^{(n)}(k + \Delta k, l + \Delta l) \right)}{a_{l_1, i}^{(n)}(k, l) + a_{l_2, i}^{(n)}(k, l)} \quad (20)$$

Comparing the match measure to a threshold th determines if detail coefficients are to be combined by simple selection or by weighted averaging. The associated weights for fusion are given by

$$\lambda_i^{(n)}(k, l) = \begin{cases} 1 & m_{l_1, l_2, i}^{(n)}(k, l) \leq th, a_{l_1, i}^{(n)}(k, l) > a_{l_2, i}^{(n)}(k, l) \\ 0 & m_{l_1, l_2, i}^{(n)}(k, l) \leq th, a_{l_1, i}^{(n)}(k, l) \leq a_{l_2, i}^{(n)}(k, l) \\ \frac{1}{2} + \frac{1}{2} \left(\frac{1 - m_{l_1, l_2, i}^{(n)}(k, l)}{1 - T} \right) & m_{l_1, l_2, i}^{(n)}(k, l) > th, a_{l_1, i}^{(n)}(k, l) > a_{l_2, i}^{(n)}(k, l) \\ \frac{1}{2} - \frac{1}{2} \left(\frac{1 - m_{l_1, l_2, i}^{(n)}(k, l)}{1 - T} \right) & m_{l_1, l_2, i}^{(n)}(k, l) > th, a_{l_1, i}^{(n)}(k, l) \leq a_{l_2, i}^{(n)}(k, l) \end{cases} \quad (21)$$

For each of the i high-pass sub-bands at each level of decomposition n , the detail coefficients for the fused image F are again determined by (18).

4. Region-based fusion using multi-resolution decomposition schemes

Pixel-based image fusion approaches determine the detail coefficients of a fused image on a per pixel basis. Namely, they use the transform data at local neighborhoods to individually determine each detail coefficient of the ultimate fusion result. Applications which utilize image fusion schemes are by in large more interested in fusing the various objects found in the original source images. This suggests that information regarding feature instead of the pixels themselves should be incorporated into the fusion process. This provides the motivation for region-based image fusion algorithms (Piella, 2003). Region-based fusion algorithms use image segmentation to guide the fusion process. A generalized region-based multi-resolution fusion algorithm is illustrated in Figure 4. The source images are once again first transformed using a given multi-resolution decomposition scheme. They are segmented using a segmentation algorithm, yielding a shared region representation which is thereby used to aid the fusion of detail coefficients at each scale. The detail coefficients in each region at each scale are fused based on their level of activity in the given region. The fusion of approximation coefficients at the highest level of decomposition remains unchanged. The result is a more robust fusion approach which can overcome blurring effects and improve sensitivity to noise and misregistration known in pixel-based approaches. Moreover, region-based image fusion have allowed for a broader class of fusion rules to be formulated. The choice of segmentation algorithm used in region-based image fusion directly affects the fusion result. Segmentation algorithms which have been used in region-based image fusion algorithms include watershed (Lewis et al., 2004), K-means (Khan et al., 2007), texture-based (Li et al., 2003), pyramidal linking (Piella, 2003), and mean-shift segmentation (Shuang & Zhilin, 2008). In this paper, mean-shift segmentation is used for all region-based approaches because of its robustness and because it has previously been applied for image fusion purposes yielding promising results. It may be substituted with another segmentation algorithm. As this paper is primarily concerned with the use of the nonlinear frameworks and multi-resolution schemes for image fusion, a discussion of appropriate segmentation algorithms for image fusion is considered outside of the scope of this work. The main objective here is to ultimately extend the use of parameterized logarithmic image fusion to region-based approaches.

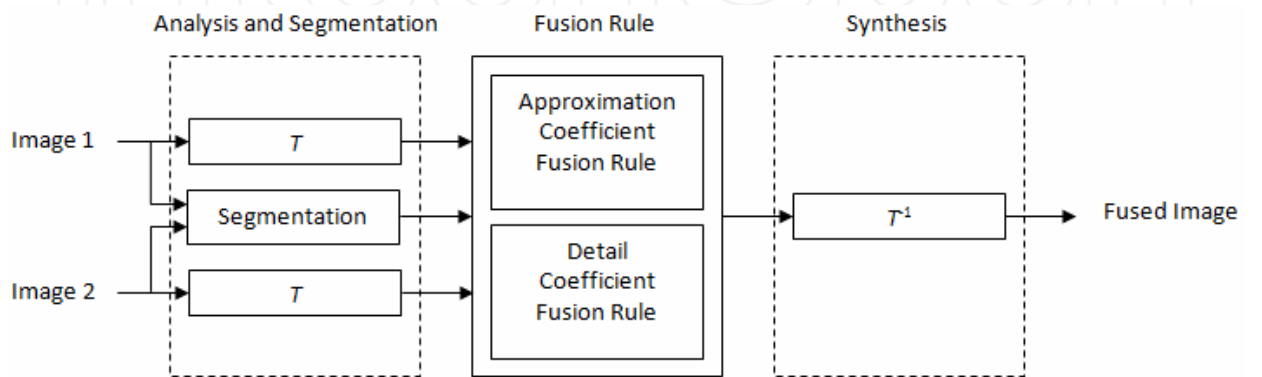


Fig. 4. A generalized region-based multi-resolution image fusion algorithm

4.1 Mean-shift segmentation

Mean-shift segmentation is a specific application of the mean-shift procedure (Comanicu & Meer, 2002). The mean shift procedure is an adaptive gradient ascent which can be used for mode detection, and is thus a nonparametric tool for feature space analysis. Given a radially symmetric kernel $K(x)$ with a monotonically decreasing profile function $k(x)$, the kernel $G(x)$ is defined as a kernel with profile function

$$g(x) = -k'(x) \quad (22)$$

For n data points $x_i, i = 1, \dots, n$, the mean shift is defined by

$$m_{h,G}(x) = \frac{\sum_{i=1}^n x_i g\left(\left\|\frac{x-x_i}{h}\right\|^2\right)}{\sum_{i=1}^n g\left(\left\|\frac{x-x_i}{h}\right\|^2\right)} - x \quad (23)$$

where h is a bandwidth parameter and x is the center of the kernel G . The mean shift procedure iteratively calculates the center position of the kernel G by

$$y_{j+1} = \frac{\sum_{i=1}^n x_i g\left(\left\|\frac{y_j-x_i}{h}\right\|^2\right)}{\sum_{i=1}^n g\left(\left\|\frac{y_j-x_i}{h}\right\|^2\right)} \quad (24)$$

The procedure is guaranteed convergence, which is arrived when the estimate has a gradient of zero. By representing images as a 2D lattice of p -dimensional vectors, where $p = 1$ corresponds to grayscale, $p = 3$ corresponds to color, and $p > 3$ corresponds to multispectral images, the space of the lattice can be referred to as the spatial domain and the gray level, color, or spectral data can be referred to as the range domain. Accordingly, a multi-variate kernel K can be defined by

$$K_{h_s, h_r}(x) = \frac{C}{h_s^2 h_r^p} k\left(\left\|\frac{x^s}{h_s}\right\|^2\right) k\left(\left\|\frac{x^r}{h_r}\right\|^2\right) \quad (25)$$

where h_s is a spatial bandwidth parameter, h_r is a range bandwidth parameter, and C is a normalizing constant. Accordingly, a mean-shift filtering is proposed, where each pixel is mapped to its spatial and range convergence point. The mean-shift segmentation merges results from the mean-shift filtering algorithm by grouping pixels whose resulting convergence points are closer than h_s in the spatial domain and h_r in the range domain. Therefore, the h_s and h_r parameters are the only user selected parameters for the segmentation (Tao et al. 2007). A shared region representation for region-based image fusion purposes is yielded using mean-shift segmentation by individually segmenting each of the source images, and by then splitting overlapping regions into new regions. An example of a shared region representation yielded using mean-shift segmentation is shown in Figure 5. To maintain consistency in segmentation results across different scales, successive down-

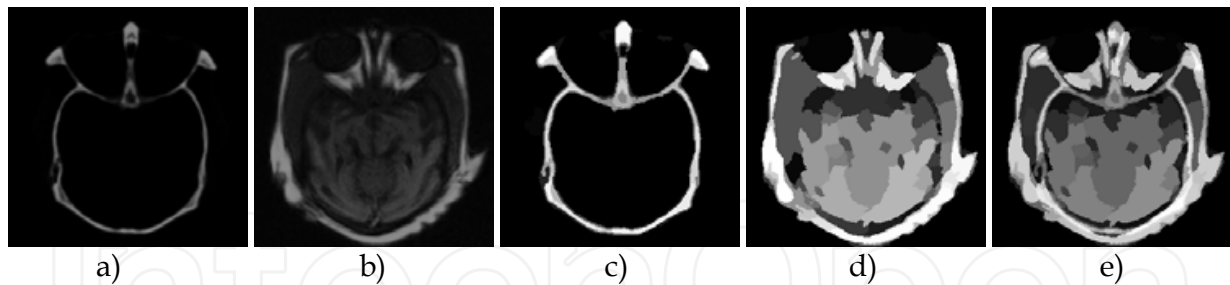


Fig. 5. (a)(b) Original “brain” source images, (c) mean-shift segmentation result of (a), (d) mean-shift segmentation result of (b), (e) shared region representation for region-based image fusion

sampling is performed to yield a shared region representation at each level of decomposition based on the image decomposition scheme used for image fusion.

4.2 Region-based detail coefficient fusion rules

Most any fusion rule formulated for pixel-based fusion can be easily formulated in terms of regions. The extension to regions merely involves calculating activity measures, match measures, and fusion weights for each region R instead of each pixel (Piella, 2003). For example, the activity measure for each region of each sub-band i of each source image can be defined by

$$a_{l,i}^{(n)}(R) = \sum_{(k,l) \in R} \left(y_{l,i}^{(n)}(k,l) \right)^2 \quad (26)$$

where $|R|$ is the area of the region R . Similarly, the match measure $m_{l_1,l_2,i}^{(n)}(R)$ and the multiplicative fusion weight $\lambda_i^{(n)}(R)$ for each region of each sub-band i can be defined. For each of the i high-pass sub-bands at each level of decomposition n , the detail coefficients of the fused image F in each region R are determined by

$$y_{F,i}^{(n)}(R) = \lambda_i^{(n)}(R) y_{l_1,i}^{(n)}(R) + (1 - \lambda_i^{(n)}(R)) y_{l_2,i}^{(n)}(R) \quad (27)$$

5. Parameterized logarithmic image processing (PLIP) model

5.1 Formulation

The LIP model was originally developed to provide a representation and processing framework for images in a bounded intensity range which is consistent with the physical laws of image combination and amplification. The model processes images as absorption filters known as graytones based on M , the maximum value of the range of I , and is characterized by its isomorphic transformation which mathematically emulates the relevant nonlinear physical model which the LIP model is based on. A new set of LIP mathematical operators, namely addition, subtraction, and scalar multiplication, are consequently defined for graytones g_1 and g_2 and scalar constant c in terms of this isomorphic transformation, thus replacing traditional mathematical operators with nonlinear operators which attempt to characterize the nonlinearity of image arithmetic (Jourlin & Pinoli, 2001). For example, LIP addition emulates the intensity image projected onto a screen when a uniform light source is filtered by two graytones placed in series. Subsequently, LIP convolution is also defined for

a graytone g and filter w (Palomares et al., 2005). The framework is consistent with several properties of the human visual system, such as brightness range inversion, Weber’s law, saturation characteristics, and the psychophysical notion. However, it has been shown that psychophysical laws can be context-dependent, and thus, the constants governing these psychophysical laws are indeed parametric (Krueger, 1989). Thus, the PLIP model generalizes the concept of nonlinear image processing frameworks initially proposed in the form of the LIP model by adding parameterization to the model.

Table 1 summarizes and compares the LIP and PLIP mathematical operators. In its most general form, the PLIP model generalizes graytone calculation, arithmetic operations, and the isomorphic transformation independently, giving rise to the model parameters μ , γ , k , λ , and β . To reduce the number of parameters needed for image fusion, this paper considers the specific instance in which $\mu = M$, $\gamma = k = \lambda$, and $\beta = 1$, effectively resulting in a single model parameter γ . In this case, The PLIP model generalizes the isomorphic transformation which defines the LIP model by accordingly choosing values for γ . Practically, for images in $[0, M)$, the value of γ can either be chosen such that $\gamma \geq M$ for positive γ or can take on any negative value. The resulting PLIP mathematical operators based on the parameterized isomorphic transformation can be subsequently derived.

	LIP Model	PLIP Model
Graytone	$g = M - I$	$g = \mu - I$
Addition	$g_1 \triangle g_2 = g_1 + g_2 - \frac{g_1 g_2}{M}$	$g_1 \tilde{\oplus} g_2 = g_1 + g_2 - \frac{g_1 g_2}{\gamma}$
Subtraction	$g_1 \triangle g_2 = M \frac{g_1 - g_2}{M - g_2}$	$g_1 \tilde{\ominus} g_2 = k \frac{g_1 - g_2}{k - g_2}$
Scalar Multiplication	$c \triangle g_1 = M - M \left(1 - \frac{g_1}{M} \right)^c$	$c \tilde{\otimes} g_1 = \gamma - \gamma \left(1 - \frac{g_1}{\gamma} \right)^c$
Isomorphic Transformation	$\varphi(g) = -M \ln \left(1 - \frac{g}{M} \right)$ $\varphi^{-1}(g) = -M \left[1 - \exp \left(-\frac{g}{M} \right) \right]$	$\tilde{\varphi}(g) = -\lambda \cdot \ln^\beta \left(1 - \frac{g}{\lambda} \right)$ $\tilde{\varphi}^{-1}(g) = \lambda \left[1 - \exp \left(\frac{-g}{\lambda} \right)^{\frac{1}{\beta}} \right]$
Graytone Multiplication	$g_1 \triangle g_2 = \varphi^{-1} \left(\varphi(g_1) \varphi(g_2) \right)$	$g_1 \tilde{\bullet} g_2 = \tilde{\varphi}^{-1} \left(\tilde{\varphi}(g_1) \tilde{\varphi}(g_2) \right)$
Convolution	$u \triangle g = \varphi^{-1} \left(w * \varphi(g) \right)$	$w \tilde{*} g = \tilde{\varphi}^{-1} \left(w * \tilde{\varphi}(g) \right)$

Table 1. Summary of the LIP and PLIP operators

5.2 Properties

The PLIP properties to be discussed refer to the specific instance of the PLIP model in which $\mu = M$, $\gamma = k = \lambda$, and $\beta = 1$. Similar intuitions are deduced for the more general cases.

1. The PLIP model operators revert to the LIP model operators with $\gamma = M$.
2. It can be shown that

$$\lim_{|\gamma| \rightarrow \infty} \tilde{\varphi}(a) = \lim_{|\gamma| \rightarrow \infty} \tilde{\varphi}^{-1}(a) = a$$

(28)

Since $\tilde{\varphi}$ and $\tilde{\varphi}^{-1}$ are continuous functions, the PLIP model operators revert to arithmetic operators as $|\gamma|$ approaches infinity and therefore, the PLIP model approaches standard linear processing of graytone functions as $|\gamma|$ approaches infinity. Depending on the nature of the algorithm, an algorithm which utilizes standard linear processing operators can be found to be an instance of an algorithm using the PLIP model with $\gamma = \infty$.

3. The PLIP model can generate intermediate cases between LIP operators and standard operators by choosing γ in the range (M, ∞) .
4. For input graytones in $[0, M)$, the range of PLIP addition and multiplication with γ in $[M, \infty]$ is $[0, \gamma]$.
5. For input graytones in $[0, M)$, the range of PLIP subtraction with γ in $[M, \infty]$ is $(-\infty, \gamma]$.
6. It can be shown that the PLIP operators obey the associative, commutative, and distributive laws and unit identities.
7. The operations satisfy the 4 requirements for image processing frameworks (Jourlin & Pinoli, 2001) and an additional 5th one. Namely, (1) the image processing framework must be based on a physically relevant image formation model; (2) The mathematical operations must be consistent with the physical nature of images; (3) The operations must be computationally effective; (4) The framework must be practically fruitful; (5) The framework must minimize the loss of information.



Fig. 6. (a) "Lena" image , (b) "Cameraman" image, image addition using (c) $\gamma = 256$ (LIP model case), (d) $\gamma = 300$, (e) $\gamma = 600$, (f) $\gamma = 10^8$

The 5th requirement essentially states that when visually "good" images are processed, the output must also be visually "good" (Panetta et al., 2008). The PLIP model satisfies the requirements by selecting values of γ which expands the dynamic range of outputs in order

to minimize information loss while also retaining non-linear, logarithmic functionality according to a physical model. This property is illustrated in Figure 6. The LIP addition provides a good contrast between Lena and the cameraman, but there is also a loss of information in the output, namely in the area corresponding to the cameraman's coat. PLIP addition with $\gamma = 300$ is able to yield a good contrast while also minimizing loss of information. Thus, for positive γ , the PLIP model physically provides a balance between the standard linear processing model and the LIP model. Conversely, negative values of γ may be selected for cases in which added brightness is needed to yield more visually pleasing results.

6. Image fusion using the PLIP model

Adapting image fusion algorithms with the PLIP model require a mathematical formulation of multi-resolution decomposition schemes and coefficient fusion rules in terms of the model. The combination of the parameterized logarithmic image decomposition techniques with parameterized logarithmic fusion rules yields a new set of image fusion algorithms which are based on the PLIP model. The parameterized logarithmic multi-resolution decomposition schemes and fusion rules are defined for graytone functions. Therefore, images are converted to graytone functions before PLIP-based operations are performed and converted from graytone functions to images after PLIP-based operation are performed.

6.1 Parameterized logarithmic multi-scale image decomposition schemes

6.1.1 Parameterized Logarithmic Laplacian Pyramid (PL-LP)

The approximation coefficients for a graytone function g at a scale $n > 0$ are generated by

$$\tilde{y}_0^{(n)} = \left[w \tilde{*} \tilde{y}_0^{(n-1)} \right]_{\downarrow 2} \quad (29)$$

where $\tilde{y}_0^{(n)} = g$ and w is the low-pass filter defined in (2). The detail coefficients at scale n are then generated by

$$\tilde{y}_1^{(n)} = \tilde{y}_0^{(n)} \tilde{\Theta}(4w) \tilde{*} \left[\tilde{y}_0^{(n+1)} \right]_{\uparrow 2} \quad (30)$$

The inverse procedure begins from the approximation coefficient at the high decomposition level N . Each synthesis level reconstructs approximation coefficients at a scale $i < N$ by each synthesis level by

$$\tilde{y}_0^{(n)} = \tilde{y}_1^{(n)} \oplus (4w) \tilde{*} \left[\tilde{y}_0^{(n+1)} \right]_{\uparrow 2} \quad (31)$$

6.1.2 Parameterized Logarithmic Discrete Wavelet Transform (PL-DWT)

The PL-DWT at decomposition level n follows directly from (44) and (45). The PL-DWT for a graytone function g at a scale $n > 0$ is calculated by

$$\tilde{W}_{DWT}(\tilde{y}_0^{(n)}) = \tilde{\varphi}^{-1} \left(W_{DWT} \left(\tilde{\varphi}(\tilde{y}_0^{(n)}) \right) \right) \quad (32)$$

where $\tilde{y}_0^{(0)} = g$. Similarly, the inverse procedure begins from the discrete wavelet coefficients at the highest decomposition level N . Each synthesis level reconstructs approximation coefficients at a scale $i < N$ by each synthesis level by

$$\tilde{W}_{DWT}^{-1}\left(\tilde{W}_{DWT}\left(\tilde{y}_0^{(n)}\right)\right)=\tilde{\varphi}^{-1}\left(W_{DWT}^{-1}\left(\tilde{\varphi}\left(\tilde{W}_{DWT}\left(\tilde{y}_0^{(n)}\right)\right)\right)\right) \quad (33)$$

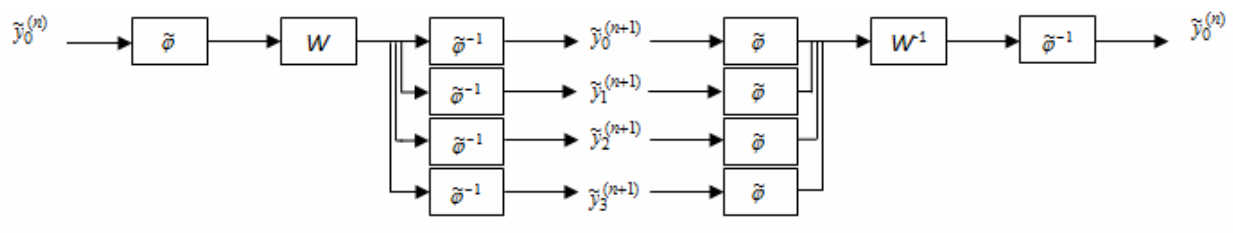


Fig. 7. Parameterized Logarithmic Wavelet Transform analysis and synthesis

6.1.3 Parameterized Logarithmic Stationary Wavelet Transform (PL-SWT)

The PL-SWT also follows directly from (44) and (45). The forward and inverse PL-SWT for a graytone function g at a scale $n > 0$ is calculated by

$$\tilde{W}_{SWT}\left(\tilde{y}_0^{(n)}\right)=\tilde{\varphi}^{-1}\left(W_{SWT}\left(\tilde{\varphi}\left(\tilde{y}_0^{(n)}\right)\right)\right) \quad (33)$$

$$\tilde{W}_{SWT}^{-1}\left(\tilde{W}_{SWT}\left(\tilde{y}_0^{(n)}\right)\right)=\tilde{\varphi}^{-1}\left(W_{SWT}^{-1}\left(\tilde{\varphi}\left(\tilde{W}_{SWT}\left(\tilde{y}_0^{(n)}\right)\right)\right)\right) \quad (34)$$

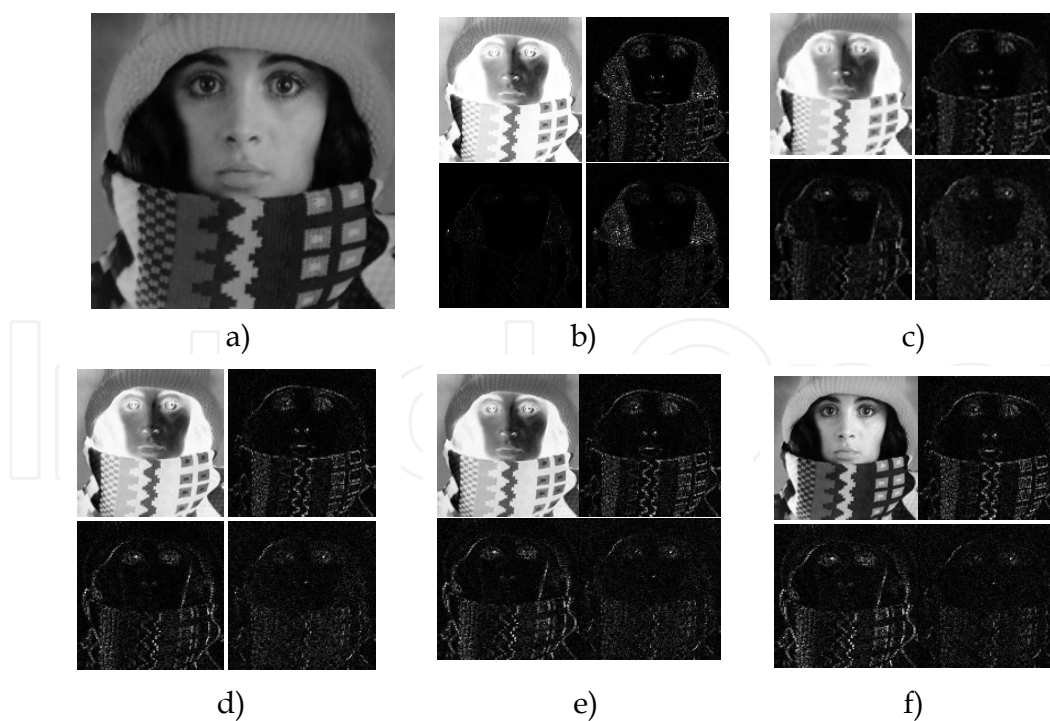


Fig. 8. (a) Original "Trui" image, top-left: approximation sub-band, magnitude of top-right: horizontal sub-band, bottom-left: vertical sub-band, bottom-right: diagonal sub-band magnitude of horizontal sub-band using the DWT and PLIP model operators with (b) $\gamma = 256$ (LIP model case), (c) $\gamma = 300$, (d) $\gamma = 500$, (e) $\gamma = 700$, (f) standard operators

Figure 7 illustrates the analysis and synthesis stages using PLIP wavelet transforms, where W is a type of wavelet transform (e.g. DWT, SWT, etc.) with a given set of wavelet filters (Courbebaisse, 2002). As the parameterized logarithmic decomposition approaches essentially makes use of standard decomposition schemes with added pre-processing and post-processing in the form of the isomorphic transformation calculations, they can be computed with minimal added computation cost.

Figure 8 illustrates the advantages yielded using parameterized logarithmic multi-resolution schemes. The wavelet decomposition using $\gamma = 256$ (LIP model case) predominantly extracts the hair features from the image. As γ increases, it is particularly apparent that the hair textures are less emphasized and that the scarf, hat, and facial edges and textures are more emphasized. The wavelet decomposition using standard operators extracts the most texture and edge information from the scarf, hat, and face in the image, and close to none of the texture of the hair. Visually, it is seen that the wavelet decomposition using the PLIP model operators with $\gamma = 300$ provides the best balance between extracting the hair, scarf, hat, and facial features in the image. Ultimately, the salient features which need to be extracted at each scale for further processing are task and image dependent, and thus, the PLIP model parameter can be tuned accordingly.

6.2 Parameterized Logarithmic image fusion rules

Both the approximation coefficient and detail coefficient fusion rules should also be adapted according to the PLIP model. For $\tilde{y}_{I_1,0}^{(N)}$ and $\tilde{y}_{I_2,0}^{(N)}$, the approximation coefficient sub-bands of images I_1 and I_2 , respectively, at the highest decomposition level N yielded using a given parameterized logarithmic multi-resolution decomposition technique, the approximation coefficients for the fused image F at the highest level of decomposition using simple averaging is given by

$$\tilde{y}_{F,0}^{(N)} = \frac{1}{2} \tilde{\otimes} \left(\tilde{y}_{I_1,0}^{(N)} \tilde{\oplus} \tilde{y}_{I_2,0}^{(N)} \right) \quad (35)$$

In general, an approximation coefficient fusion rule can be adapted according to the PLIP model by

$$\tilde{y}_{F,0}^{(N)} = \tilde{\varphi}^{-1} \left(R_A \left(\tilde{\varphi} \left(\tilde{y}_{I_1,0}^{(N)} \right), \tilde{\varphi} \left(\tilde{y}_{I_2,0}^{(N)} \right) \right) \right) \quad (36)$$

where R_A is an approximation coefficient fusion rule implemented using standard arithmetic operators. An analysis of the PLIP operation in Table 1 and (35) yields a simple interpretation of the effect of γ on fusion results. Practically, γ can be interpreted as a brightness parameter, where negative values of γ yield brighter fusion results and positive values of γ yield darker fusion results. This is achieved while also maintaining the fusion identity that the fusion of identical source images is the source image itself. Therefore, improved visual quality is achieved within an image fusion context and not as a result of an independent image enhancement process. The influence of the parameterization on fusion results is not limited to this naïve observation, however, as γ also influences the multi-scale decomposition scheme and the detail coefficient fusion rule. The fusion rules for details coefficients at each decomposition level for pixel- or region-based approaches are similarly adapted according to the PLIP model via the parameterized isomorphic transformation. In general, a detail coefficient fusion rule can be adapted according to the PLIP model by

$$\tilde{y}_{F,i}^{(n)} = \tilde{\varphi}^{-1}\left(R_D\left(\tilde{\varphi}\left(\tilde{y}_{I_1,i}^{(n)}\right), \tilde{\varphi}\left(\tilde{y}_{I_2,i}^{(n)}\right)\right)\right)$$

(37)

where R_D is a pixel- or region-based detail coefficient fusion rule implemented using standard arithmetic operators.

7. Quantitative image fusion quality assessment

When an ideal fusion result is available, it can be used as a reference image to guide image fusion quality assessment. Measures such as the root mean square error (RMSE), normalized least square error (NLSE), peak signal-to-noise ratio (PSNR), correlation (CORR), difference entropy (DE), and mutual information (MI) can be used to relate the fusion result to the reference image, thus providing a means of assessing image fusion quality (Liu et. al, 2008). These measures are summarized in Table 2 for a fusion result F given a reference image I . However, an ideal reference image is usually not known, and thus, quality assessment becomes a non-trivial task. Blind objective performance assessment of image fusion quality is still an open problem requiring more research in order to provide valuable objective evaluation (Piella, 2003). The metrics proposed in (Xydeas & Petrovic, 2000) and (Piella & Heijmans, 2003) tend to favor fusion results which transfer more edge information into fusion results, and are therefore vulnerable to noisy test cases. Conversely, mutual-information-based metrics (Qu et al., 2002) tend to favor fusion approaches which

RMSE	$\sqrt{\frac{\sum_{k=1}^K \sum_{l=1}^L [I(k,l) - F(k,l)]^2}{KL}}$	M	Maximum pixel value
NLSE	$\sqrt{\frac{\sum_{k=1}^K \sum_{l=1}^L [I(k,l) - F(k,l)]^2}{\sum_{k=1}^K \sum_{l=1}^L [I(k,l)]^2}}$	$P_I(g)$	Probability of value g in I
PSNR	$10\log_{10} \frac{KLM^2}{\sum_{k=1}^K \sum_{l=1}^L [I(k,l) - F(k,l)]^2}$	$P_F(g)$	Probability of value g in F
CORR	$\frac{2\sum_{k=1}^K \sum_{l=1}^L I(k,l)F(k,l)}{\sum_{k=1}^K \sum_{l=1}^L [I(k,l)]^2 + \sum_{k=1}^K \sum_{l=1}^L [F(k,l)]^2}$	h_{IF}	Normalized joint histogram
DE	$\left \sum_{g=0}^{M-1} P_I(g) \log_2 P_I(g) - \sum_{g=0}^{M-1} P_F(g) \log_2 P_F(g) \right $	h_I	Normalized histogram of I
MI	$\sum_{k=1}^M \sum_{l=1}^M h_{IF}(k,l) \log_2 \frac{h_{IF}(k,l)}{h_I(k,l)h_F(k,l)}$	h_F	Normalized histogram of F

Table 2. Summary of the reference-based measure for image fusion quality assessment

transfer relatively less edge information but are less sensitive to noise, such as region-based and even simple averaging approaches. Nonetheless, to gain objective perspective not on the fusion rule or standard decomposition scheme of choice, but rather the improvement of fusion results using the PLIP model, fusion results are assessed quantitatively using the Piella and Heijmans image fusion quality metric. The metric measures fusion quality based on how much the fusion result reflects the original source images. Bovik's quality index (Wang, 2002) is used to relate the fused result to its original source images. The quality index Q_0 proposed by Bovik to measure the similarity between two sequences x and y is given by

$$Q_0 = \frac{\sigma_{xy}}{\sigma_x \sigma_y} \cdot \frac{2\mu_x \mu_y}{\mu_x^2 + \mu_y^2} \cdot \frac{2\sigma_x \sigma_y}{\sigma_x^2 + \sigma_y^2} \quad (38)$$

where σ_x and σ_y are the sample standard deviations of x and y , respectively, σ_{xy} is the sample covariance of x and y , and μ_x and μ_y are the sample means of x and y , respectively. For two images I and F , a sliding window technique is utilized to calculate the quality index $Q_0(I, F|w)$ at each local $w \times w$ window. The average of these quality indexes is used to measure the similarity between I and F , and is given by

$$Q_0(I, F) = \frac{1}{|W|} \sum_{w \in W} Q_0(I, F|w) \quad (39)$$

The resulting similarity index ranges from 0 to 1, with two identical images yielding a Q_0 equal to 1. Defining $s(I|w)$ as the saliency, and in this case, the variance of the image I in a local window $w \times w$ window, the quality of the fused result can be assessed by first calculating local weights $\lambda(w)$ for the source images I_1 and I_2 , given by

$$\lambda(w) = \frac{s(I_1|w)}{s(I_1|w) + s(I_2|w)} \quad (40)$$

and then calculating the fusion quality index $Q(I_1, I_2, F)$ for the fused result F by

$$Q(I_1, I_2, F) = \frac{1}{|W|} \sum_{w \in W} (\lambda(w) Q_0(I_1, F|w) + (1 - \lambda(w)) Q_0(I_2, F|w)) \quad (41)$$

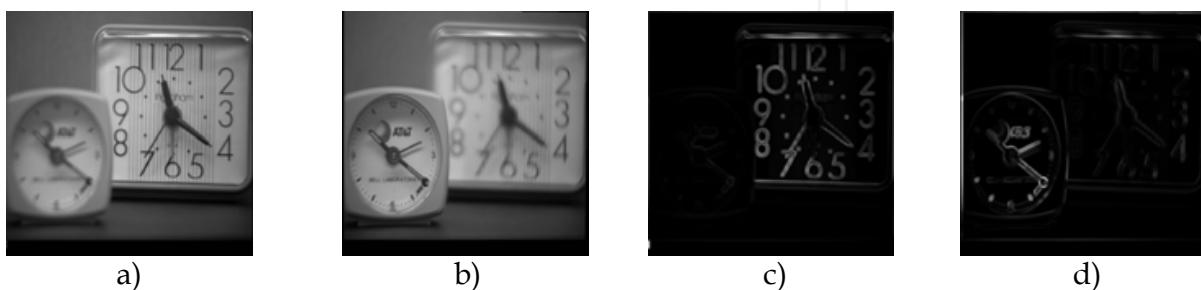


Fig. 9. (a)(b) Original “clock” source images, respective weights (c) λ (d) $c \cdot (1 - \lambda)$ used for image fusion quality assessment

The metric assesses fusion quality by calculating the local quality indexes between the fused image and the two source images, and weighting them according to the local saliency between the source images. To better reflect the human visual system, another weight is added to give more weight to regions in which the saliency of the source images is greater. Defining the overall saliency of a window $C(w)$ by

$$C(w) = \max(s(I_1 | w), s(I_2 | w)) \quad (42)$$

The weighted fusion quality index $Q_w(I_1, I_2, F)$ is given by

$$Q_w(I_1, I_2, F) = \sum_{w \in W} c(w) (\lambda(w) Q_0(I_1, F | w) + (1 - \lambda(w)) Q_0(I_2, F | w)) \quad (43)$$

where

$$c(w) = \frac{C(w)}{\sum_{w' \in W} C(w')} \quad (44)$$

As Q_0 yields a maximum value of 1 for identical input images, higher fusion quality metric values indicate better fusion results. Figure 9 provides a graphical representation of the weights which are calculated by the quality metric in order to assess the quality of image fusion results.

8. Experimental results

The effectiveness of the proposed algorithms is illustrated via computer simulations. In general, three cases are considered for these experiments: 1) the extreme case in which the PLIP model operators yield the LIP model operators ($\gamma = M$), 2) standard operators, which are the extreme case of PLIP model operators with $\gamma = \infty$, 3) the case in which γ takes on a value other than M or ∞ . For easy reference, we refer to these cases as the LIP model operator case, standard operator case, and PLIP model operator case, respectively, though in reality, all are cases of the proposed PLIP-based approach. It should be noted that image fusion algorithms employing LIP-based multi-resolution image decomposition schemes and fusion rules have not even been introduced to our knowledge. Thus, we refer to the LIP-LP, LIP-DWT, and LIP-SWT image fusion algorithms as the image fusion algorithms which use PLIP operators with $\gamma = M$ to implement the fusion rules and LP, DWT, and SWT, respectively. Consequently, the PL-LP, PL-DWT, and PL-SWT image fusion algorithms are compared to the traditional LP and LIP-LP; traditional DWT and LIP-DWT; and traditional and LIP SWT image fusion algorithms, respectively. The algorithms were tested over a range of different image classes, including out-of-focus, medical, surveillance, and remote sensing images. A portion of these results are presented here. It is assumed that the input source images are registered, although it is expected that image fusion algorithms be able to handle minor registration differences. There are many factors which influence image fusion using multi-resolution decomposition schemes, including the type of multi-resolution decomposition scheme, the number of decomposition levels, the choice of filter bank, and the fusion rule used to fuse coefficients at each scale. This paper emphasizes the transform which is used while keeping all other factors constant. In these experimental results, $N = 3$ for all methods, and both the pixel- and region-based fusion rules are examined. For the wavelet-based approaches, biorthogonal 2.2 filters are used. The fusion results are compared

quantitatively by first normalizing source images and fused results to the range 0-255, and then using the Piella and Heijmans image fusion quality metric Q_W with $w = 7$. This metric is used to determine the optimal parameter value for γ , with the resulting fused image thereby taken to be the result for a given parameterized logarithmic image fusion algorithm. This demonstrates the ability to tune the PLIP model parameter in order to optimize results according to any metric used for quality assessment.

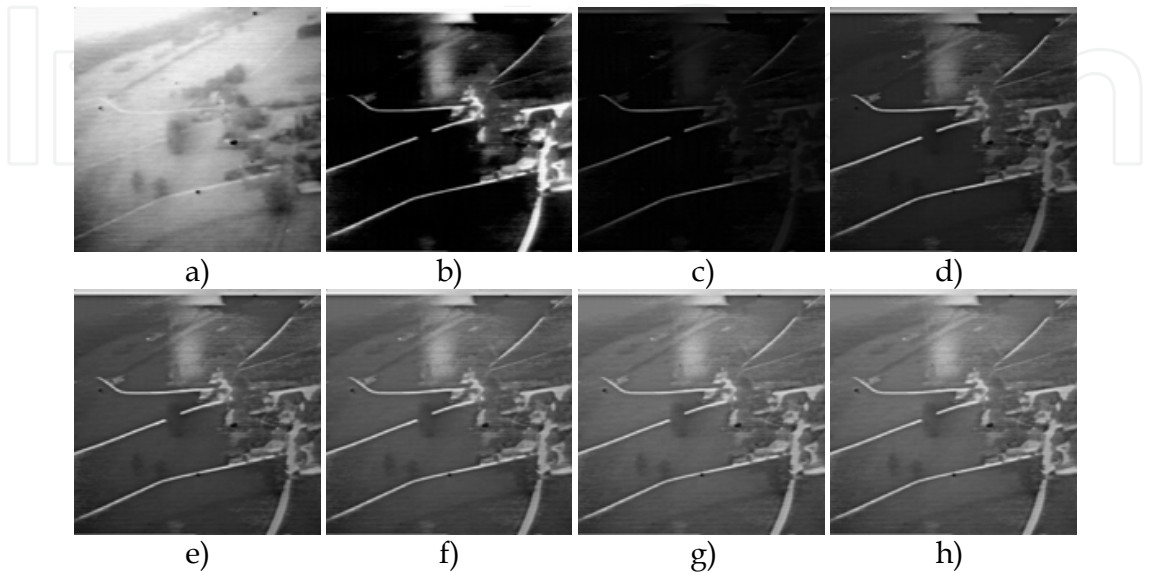


Fig. 10. (a)(b) Original “navigation” source images, image fusion results using the LP/AM fusion rule, and PLIP model operators with (c) $\gamma = 256$ (LIP model case), $Q_W = 0.3467$, (d) $\gamma = 300$, $Q_W = 0.7802$, (e) $\gamma = 430$, $Q_W = 0.8200$, (f) $\gamma = 700$, $Q_W = 0.8128$ (g) $\gamma = 10^8$, $Q_W = 0.7947$, (h) standard operators, $Q_W = 0.7947$

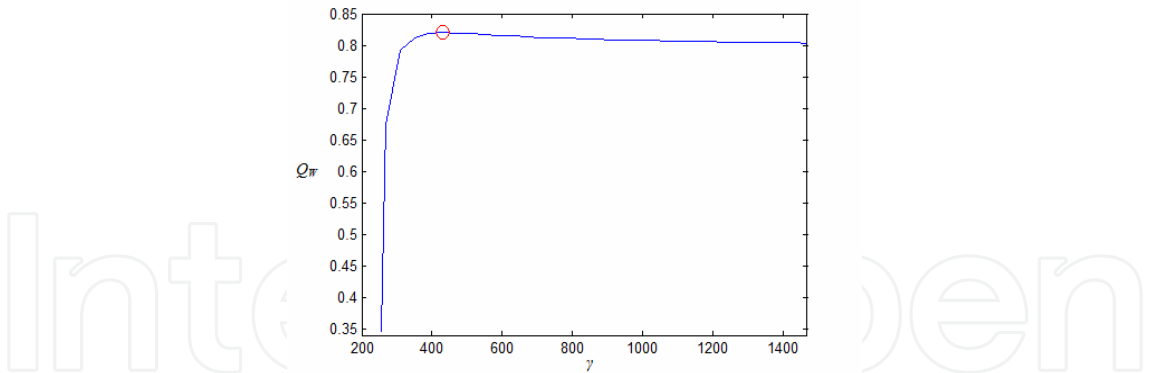


Fig. 11. Plot of Q_W vs. γ for image fusion results in Figure 9, indicating a maximum at $\gamma = 430$, $Q_W = 0.8200$

Figure 10 illustrates the fundamental themes which have been discussed so far, particularly highlighting the necessity for the added model parameterization. Figure 10.c shows that firstly, the PLIP model reverts to the LIP model with $\gamma = M = 256$, and secondly, that the combination of source images using this extreme case may still be visually unsatisfactory given the nature of the input images, even though the processing framework is based on a physically inspired model. Figure 10.d-f illustrates the way in which fusion results are affected by the parameterization, with the most improved fusion performance yielded by the proposed approach using parameterized multi-resolution decomposition schemes and

fusion rules relative to both the standard processing extreme and the LIP model extreme with $\gamma = 430$. Namely, this result using the proposed approach has better visual contrast between roads and terrain, and provides the proper base luminance to effectively differentiate between the grass and bushes. Figure 11 plots the Q_W quality metric as a function of γ , and reflects the qualitative observation indicating Figure 10.e as the best fusion output. Lastly, Figure 10 also shows using the AM fusion rule that the PLIP operators revert to standard mathematical operators as γ approaches infinity.

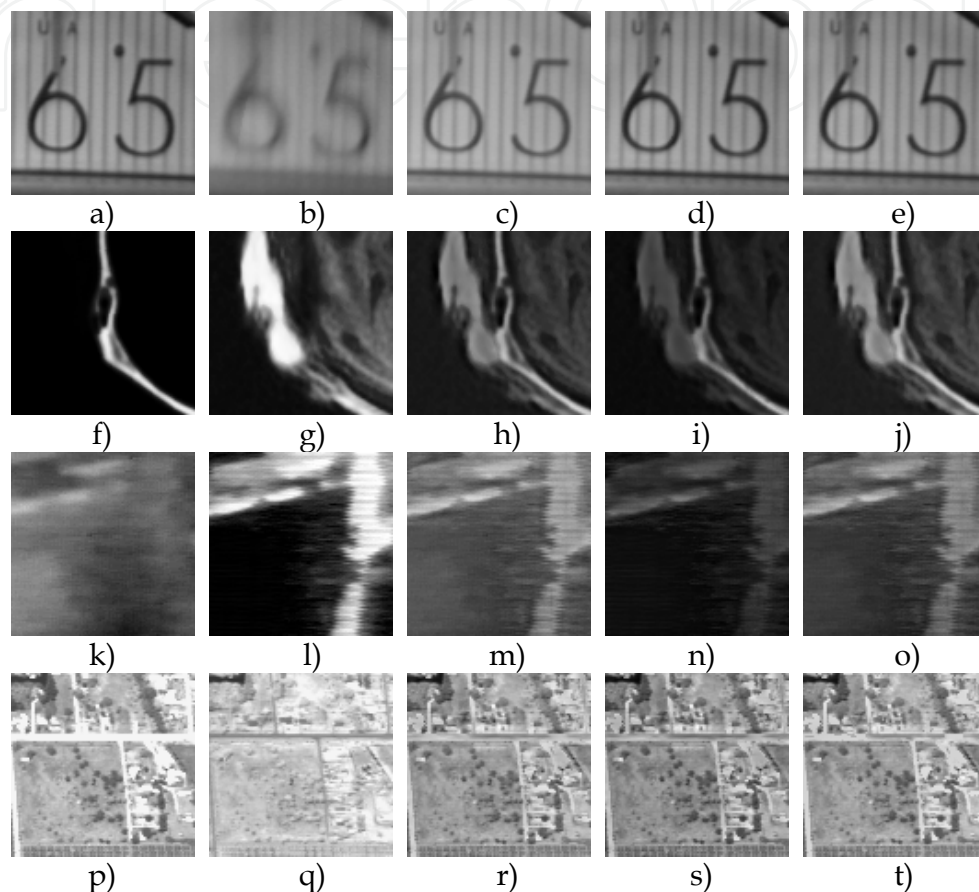


Fig. 12. Zoomed regions of (a)(b) Original “clocks” source images, image fusion results using (c)LP and RB, (d), LIP-LP and RB, (e) PL-LP and RB, (f)(g) original “brain” source images, image fusion results using (h) SWT and RB, (i) LIP-SWT and RB, (j) PL-SWT and RB (k)(l) original “navigation” source images, image fusion results using (m) DWT and AM, (n) LIP-DWT and AM, (o) PL-DWT and AM (p)(q) original “remote sensing” source images, image fusion results using (r) SWT and BK, (s) LIP-SWT and BK, (t) PL-SWT and BK

Zoomed details highlighting specific contrast differences of selected fusion results are shown in Figure 12. Selected image fusion results showing more global luminance differences can be found in Figure 13. Qualitatively, it is seen that the image fusion approaches using the PLIP model operator case yield more informative fusion results with more visually pleasing contrast. The zoomed details in the 1st row of Figure 12 show that the lines and numbers in the clock images are sharper and clearer in the fusion result using the PLIP model operator case. The 2nd row shows that the proposed method is able to better capture the terrain information and road information of the respective source images. The 3rd row shows the improved contrast of tissue information and dense bone structure yielded

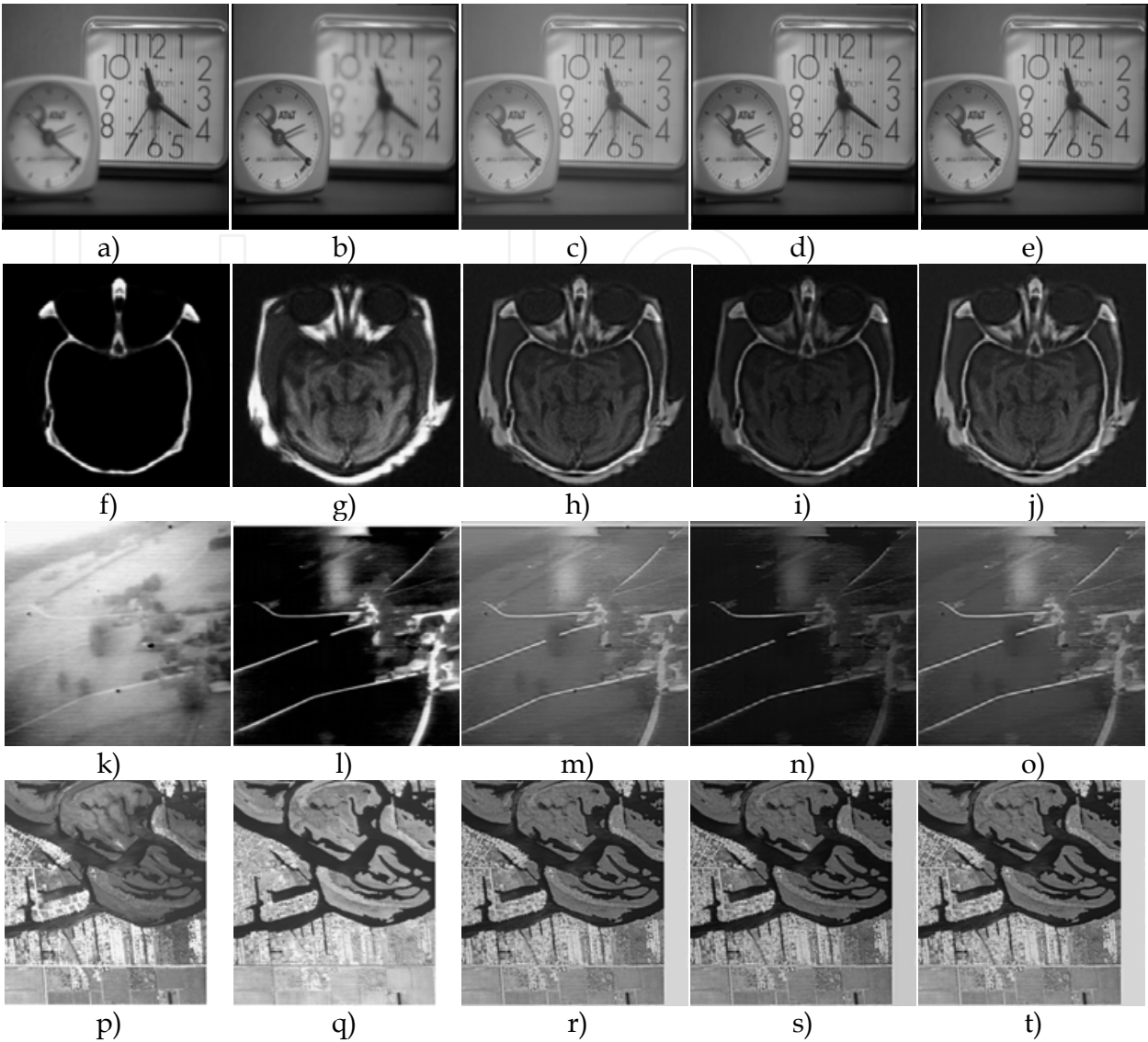


Fig. 13. (a)(b) Original “clocks” source images, image fusion results using (c)LP and RB, (d), LIP-LP and RB, (e) PL-LP and RB, (f)(g) original “brain” source images, image fusion results using (h) SWT and RB, (i) LIP-SWT and RB, (j) PL-SWT and RB (k)(l) original “navigation” source images, image fusion results using (m) DWT and AM, (n) LIP-DWT and AM, (o) PL-DWT and AM (p)(q) original “remote sensing” source images, image fusion results using (r) SWT and BK, (s) LIP-SWT and BK, (t) PL-SWT and BK

by the proposed method. Lastly, the 4th row shows that the proposed fusion approaches are able to better capture the subtle features at the point at which the roads intersect. Thus, the experimental results highlight the improvement of fusion results yielded using the PLIP model operators. While the standard operator extreme can often give adequate results, the contrast and luminance can be improved by choosing a value of γ which both reflects the human visual system and meets the dynamic range requirements of the input images. While the LIP model operator extreme can improve the performance of image fusion relative to standard operator extreme when the source images are similar in luminance (as in the case of the clocks images), it yields visually inadequate results for source images with greatly different local base luminance. This is particularly visible for input images in which one of the source images is predominantly dark as in the case of the “navigation” and “brain” images.

Table 3. Quantitative quality assessment of image fusion results using the Piella and Heijmans quality metric	SWT			DWT			LP		
	RB	BK	AM	RB	BK	AM	RB	BK	0
	0.8877	0.8926	0.8879	0.8763	0.8745	0.8750	0.8849	0.8851	0
	0.9045	0.9081	0.9085	0.8955	0.8891	0.8979	0.9114	0.9123	0
	0.9064	0.9130	0.9134	0.8972	0.8918	0.9002	0.9241	0.9250	0
	0.7458	0.7554	0.7539	0.6872	0.6701	0.7124	0.7572	0.7748	0
	0.5557	0.5714	0.5581	0.5008	0.4886	0.5296	0.5327	0.5349	0
	0.7684	0.7647	0.7718	0.7060	0.6886	0.7292	0.7576	0.7762	0
	0.7542	0.7382	0.7460	0.7288	0.7333	0.7363	0.8051	0.7933	0
	0.6873	0.7294	0.7250	0.6052	0.6064	0.6011	0.3505	0.3512	0
	0.7695	0.7821	0.7746	0.7589	0.7600	0.7607	0.8187	0.8196	0
	0.8078	0.8203	0.8137	0.7162	0.7378	0.7672	0.8113	0.8293	0
	0.7882	0.8045	0.7954	0.6869	0.6770	0.7128	0.7424	0.7627	0
	0.8080	0.8238	0.8150	0.7170	0.7385	0.7695	0.8120	0.8300	0

The quantitative observations are reflected by their corresponding quality metric values in Table 3, in which rows correspond to the basic multi-resolution decomposition scheme and fusion rule employed and columns correspond to the image processing operators (LIP model operator case, standard operator case, or PLIP model operator case) used to implement the given decomposition scheme and fusion rule. It should be noted that a single, constant-size window is used in calculating the quality metric values. Thus, such an evaluation may be dependent on how well the window size reflects the scale of the objects of interest in the source images, and may not be able to effectively quantify differences in fusion results even when qualitative visual differences are seen. This provides a rationalization as to why the perceived visual improvement of the proposed methods may in some cases only translate to a small increase in the quality metric values, and continues to affirm the fact that objective image fusion quality assessment is still an open research topic. However, the rank of the scores are generally indicative of relative performance, and to standardize the testing procedure and to maintain the same formulation of the metric as it was originally proposed, the same parameters are used to calculate quality metric values for all test cases. Thus, the quantitative analysis serves as an objective means of validating subjective observations. The quality metric values in Table 2 show that in all cases, fusion algorithms using the parameterized logarithmic multi-resolution decomposition schemes and fusion rules outperform their respective general linear processing model counterparts.

9. Conclusions

This paper derived decomposition schemes and image fusion rules based on the PLIP model. The PLIP based multi-resolution decomposition schemes were developed and thoroughly applied for image fusion purposes. PLIP model properties were analyzed, and their implications for image fusion were verified by experimental means. The new multi-resolution decomposition schemes and fusion rules yields new image fusion tools which are able to provide visually more pleasing fusion results. A new class of image fusion algorithms, namely those based on the PL-LP, PL-DWT, and PL-SWT were proposed. The images are fused in the transform domain using novel pixel-based or region-based rules. Using a number of pixel-based and region-based fusion rules, one can combine the important features of the input images in the transform domain to compose an enhanced image. The proposed algorithms were tested and compared to traditional and LIP multi-resolution image fusion algorithms over a number of different image classes including out-of-focus, medical, surveillance, and remote sensing images, whose applications can make use of image fusion to improve perception for computer-aided or computer vision systems. These experimental results showed that the proposed image decomposition and image algorithms improved image fusion quality both qualitatively and quantitatively. Qualitatively, the fusion results using the proposed algorithms provided better contrast and the necessary luminance needed for fusion purposes. Quantitatively, the proposed outperformed traditional and LIP multi-resolution image fusion algorithms using the Piella and Heijmans quality metric to objectively assess image fusion quality. The novelty of the proposed PLIP-based image fusion schemes lie in the combination of multi-resolution image fusion techniques with physically inspired processing models.

10. Acknowledgement

This work has been partially supported by NSF Grant HRD-0932339. The authors would like to thank Dr. Oliver Rockinger for kindly providing the registered images used for computer simulations.

11. References

- Burt, P.J., & Adelson, E. (1983). The Laplacian pyramid as a compact image code. *IEEE Transactions on Communications*, Vol. 31, No. 4, pp. 532-540
- Burt, P.J. & Kolczynski, R.J. (1993). Enhanced image capture through fusion, *Proceedings of the International Conference on Computer Vision*, pp. 173-1982.
- Comanicu, D. & Meer, P. (2002). Mean shift: a robust approach toward feature space analysis, *IEEE Transactions on Pattern Analysis and Machine Intelligence*, Vol. 24, (May 2002) pp. 603-619
- Courbebaisse, G.; Trunde, F., & Jourlin, M (2002). Wavelet transform and LIP model, *Image Anal Stereol*, Vol. 21, No. 2, (June 2002) pp. 121-125
- Chavez, P.S. & Kwarteng, A.Y. (1989). Extracting spectral contrast in Landsat Thematic Mapper image data using selective component analysis, *Photogrammetric Engineering and Remote Sensing*, Vol. 55, No. 3, pp. 339-348
- Chibani, Y. (2005). Selective synthetic aperture radar and panchromatic image fusion by using the a trous wavelet decomposition. *EURASIP Journal on Applied Signal Processing*, Vol. 2005, No. 14, pp. 2007-2214
- Daneshvar, S. & Ghassemian, H. (2010). MRI and PET image fusion by combining IHS and retina-inspired model. *Information Fusion*, Vol. 11, No. 2, (April 2010) pp. 114-123
- Debayle, J.; Gavet, Y. & Pinoli, J.C. (2006). General adaptive neighbourhood image restoration, enhancement and segmentation, *Image Analysis and Recognition*, pp. 29-40
- Deng G.; Cahill L.W., & Tobin, G.R. (2009). The study of logarithmic image processing model and its application to image enhancement. *IEEE Transactions on Image Processing*, Vol. 18, pp. 1135-1140
- Fowler, J.E. (2005). The redundant discrete wavelet transform and additive noise. *IEEE Signal Processing Letters*, Vol. 12, No. 9, pp. 629-632
- Hill, P.; Canagarajah, N. & Bull, D. (2002). Image fusion using complex wavelets, *Proceedings of the British Machine Vision Conference*, pp. 487-496
- Jourlin, M. & Pinoli, J. (2001). Logarithmic image processing: the mathematical and physical framework for the representation and processing of transmitted images. *Advances in Imaging and Electron Physics*, Vol. 115, pp. 126-196
- Khan, A.M.; Kayani, B. & Gillani, A.M. (2007). Feature level fusion of night vision images based on K-means clustering algorithm, *Innovations and Advanced Techniques in Computer and Information Sciences and Engineering*, pp. 73-76.
- Lewis, J.J.; O'Callaghan, R.J., Nikolov, S.G., Bull, D.R. & Canagarajah, C.N. (2004). Region-based image fusion using complex wavelets, *Proceedings of the International Conference on Image Fusion*, pp. 2004, July 2004
- Li., Z.; Jing, Z., Liu, G., Sun, S. & Leung, H. (2003). A region-based image fusion algorithm using multiresolution segmentation, *Proceedings of the IEEE International Conference on Intelligent Transportation Systems*, Vol. 1, pp. 96-101

- Krueger, L. (1989). Reconciling Fechner and Stevens: toward a unified psychophysical law, *Behavioral and Brain Sciences*, Vol. 12, pp. 251-267
- Kumar, M. & Dass, S. (2009). A total variation-based algorithm for pixel-level image fusion. *IEEE Transactions on Image Processing*, Vol. 18, No. 9, (September 2009) pp. 2137-2143
- Mallat, S.G. (1989). A theory for multiresolution signal decomposition: the wavelet representation. *IEEE Transactions on Pattern Analysis and Machine Intelligence*, Vol. 11, (July 1989) pp. 674-693
- Palomares, J.M.; Gonzalez, J. & Ros, E. (2005). Designing a fast convolution under the LIP paradigm applied to edge detection, *Proceedings of the International on Advances in Pattern Recognition*, pp. 560-569.
- Panetta, K.; Wharton, E. & Agaian, S. (2008). Human visual system based image enhancement and logarithmic contrast measure. *IEEE Transactions on Systems, Man, and Cybernetics, Part B: Cybernetics*, Vol. 38, No. 1, (February 2008) pp. 174- 188
- Piella, G. (2003). A general framework for multiresolution image fusion: from pixels to regions. *Information Fusion*, Vol. 4, pp. 259-280
- Piella, G. & Heijmans, H. (2003). A new quality metric for image fusion, *Proceedings of the IEEE International Conference on Image Processing*, ISBN 1522-4880, September 2003
- Pinoli, J.C. (1997). A general comparative study of the multiplicative homomorphic, log-ratio, and logarithmic image processing approaches, *Signal Processing*, Vol. 58, pp. 11-45
- Qiong, Z.; Sheng, Z. & Zhao, Y. (2008). Dynamic infrared and visible image sequence fusion based on DT-CWT using GGD, *Proceedings of the IEEE International Conference on Computer Science and Information Technology*, Singapore, ISBN 978-0-7695-3308-7, August 2008
- Qu, G.H.; Zhang, D.L. & Yan, P.F. (2002). Information measure for performance of image fusion, *Electronic Letters*, Vol. 38, No. 7, pp. 313-315
- Rockinger, O. (1997). Image sequence fusion using a shift-invariant wavelet transform, *Proceedings of the IEEE International Conference on Image Processing*, pp. 288-291
- Shuang, L. & Zhilin, L. (2008). A Region-based technique for fusion of high-resolution images using mean shift segmentation, *International Archives of the Photogrammetry, Remote Sensing, and Spatial Information Sciences*, Vol. 38, pp. 1267-1272
- Tabb, M. & Ahuja, N. (1997). Multiscale image segmentation by integrated edge and region detection, *IEEE Transactions on Image Processing*, Vol. 6, No. 5, (May 1997) pp. 642-655
- Tao, W.; Jin, H. & Chang, Y. (2007). Color image segmentation based on mean shift and normalized cuts, *IEEE Transactions on Systems, Man, and Cybernetics, Part B: Cybernetics*, Vol. 37, No. 5, (October 2007) pp. 1382-1389
- Tu, T.M.; Su, S.C., Shyu, H.C. & Huang, P.S. (2001). Efficient intensity-hue-saturation-based image fusion with saturation compensation, *SPIE Optical Engineering*, Vol. 40, No. 720.
- Wang, Z. (2008). Medical image fusion using m-PCNN, *Information Fusion*, Vol. 9, No. 2, (April 2008) pp. 176-185.
- Wang, Z. & Bovik, A.C. (2002). A universal image quality index, *IEEE Signal Processing Letters*, Vol. 9, No. 3, pp. 81-84.

- Wharton, E.; Agaian, S. & Panetta, K. (2006). Comparative study of logarithmic enhancement algorithms with performance measure, *Proceedings of SPIE Conference on Electronic Imaging: Algorithms and Systems, Neural Networks, and Machine Learning*, Vol. 6064
- Wharton, E.; Panetta, K. & Agaian S. (2007). Logarithmic edge detection with applications, *Proceedings of IEEE International Conference on Systems, Man, and Cybernetics*, pp. 3346-3351, October 2007.
- Xydeas C.S. & Petrovic, V. (2000). Objective image fusion performance measure, *Electronic Letters*, Vol. 36, No. 4, (February 2000) pp. 308-309
- Yang, Y.; Park D.S., Huang S. & Rao N. (2010). Medical image fusion via an effective wavelet-based approach. *EURASIP Journal on Advances in Signal Processing*, Vol. 2010, No. 10115
- Zhang, Z. & Blum, R. (1999). A categorization of multiscale-decomposition-based image fusion schemes with a performance study for a digital camera application. *Proceedings of the IEEE*, Vol. 87, No. 8, (August 1999) pp. 1315-1326
- Zhang, Z. & Blum, R. (1997). Region-based image fusion scheme for concealed weapon detection, *Proceedings of the Conference on Information Sciences and Systems*, pp. 168-173.
- Zheng, L.; Forsyth, D. & Laganieri, R. (2008). A feature-based metric for the quantitative evaluation of pixel-level image fusion, *Computer Vision and Image Understanding*, Vol. 109, No. 1, (January 2008) pp. 56-68

IntechOpen

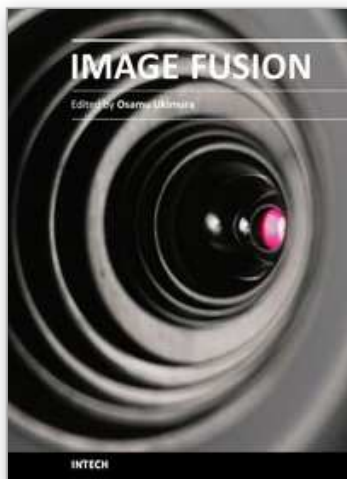


Image Fusion

Edited by Osamu Ukimura

ISBN 978-953-307-679-9

Hard cover, 428 pages

Publisher InTech

Published online 12, January, 2011

Published in print edition January, 2011

Image fusion technology has successfully contributed to various fields such as medical diagnosis and navigation, surveillance systems, remote sensing, digital cameras, military applications, computer vision, etc. Image fusion aims to generate a fused single image which contains more precise reliable visualization of the objects than any source image of them. This book presents various recent advances in research and development in the field of image fusion. It has been created through the diligence and creativity of some of the most accomplished experts in various fields.

How to reference

In order to correctly reference this scholarly work, feel free to copy and paste the following:

Sos S. Agaian, Karen A. Panetta and Shahan C. Nercessian (2011). Image Fusion Using a Parameterized Logarithmic Image Processing Framework, Image Fusion, Osamu Ukimura (Ed.), ISBN: 978-953-307-679-9, InTech, Available from: <http://www.intechopen.com/books/image-fusion/image-fusion-using-a-parameterized-logarithmic-image-processing-framework>

INTECH
open science | open minds

InTech Europe

University Campus STeP Ri
Slavka Krautzeka 83/A
51000 Rijeka, Croatia
Phone: +385 (51) 770 447
Fax: +385 (51) 686 166
www.intechopen.com

InTech China

Unit 405, Office Block, Hotel Equatorial Shanghai
No.65, Yan An Road (West), Shanghai, 200040, China
中国上海市延安西路65号上海国际贵都大饭店办公楼405单元
Phone: +86-21-62489820
Fax: +86-21-62489821

© 2011 The Author(s). Licensee IntechOpen. This chapter is distributed under the terms of the [Creative Commons Attribution-NonCommercial-ShareAlike-3.0 License](https://creativecommons.org/licenses/by-nc-sa/3.0/), which permits use, distribution and reproduction for non-commercial purposes, provided the original is properly cited and derivative works building on this content are distributed under the same license.

IntechOpen

IntechOpen